AIAA AVIATION Forum
13-17 June 2016, Washington, D.C.
32nd AIAA Aerodynamic Measurement Technology and Ground Testing Conference

10.2514/6.2016-3655

Wind Tunnel Support System Influence on NASA Common Research Model at Low Speed Conditions

Andreas Waldmann[*], Thorsten Lutz[†] and Ewald Krämer[‡]

University of Stuttgart, 70569 Stuttgart, Germany

Computational studies were conducted in order to gain an understanding and to quantify the impact of the model support system and aeroelastic wing deformation on the Common Research Model at subsonic inflow conditions at $Re_\infty = 11.6 \cdot 10^6$. Comparisons between results obtained in the European Transonic Windtunnel and from simulations using TAU reveal the extent of the modeling error introduced by neglecting the support structure. RANS simulations with and without the support system show that it has a near-field effect on the model's rear fuselage, significantly altering the pressure field and thereby impacting the force coefficients, most significantly drag and pitching moment. Aeroelastic wing deformation was also included in the investigation, showing non-negligible impact on the forces. The inclusion of the support system and wing deformation, as well as the use of advanced turbulence models, were shown to promise considerable error reduction potential in comparative studies between wind tunnel and simulation data.

Nomenclature

b	wing span
c	wing chord
C_D	drag coefficient
C_L	lift coefficient
C_M	pitching moment coefficient with respect to the model reference point
c_p	pressure coefficient
c_f	friction coefficient
M	Mach number
Re	Reynolds number
q/E	dynamic pressure normalized with Young's modulus
y^+	normalized wall distance
α	angle of attack
η	normalized spanwise coordinate, $\eta = y/(0.5b)$
Θ	local wing twist in degrees
∞	subscript denoting freestream conditions

I.   Introduction

DESPITE the advances made in the field of computational fluid dynamics (CFD), wind tunnel tests of commercial aircraft configurations are still indispensable when high quality lift and drag measurements are sought. Ensuring comparability between numerical and experimental data is paramount, because both approaches complement each other. Computational results are usually obtained using far field boundary conditions that resemble free flight. Conversely, wind tunnel measurements are affected by the presence of

[*]Research Engineer, Institute of Aerodynamics and Gas Dynamics, Pfaffenwaldring 21, AIAA member
[†]Senior Researcher, Institute of Aerodynamics and Gas Dynamics, Pfaffenwaldring 21
[‡]Professor, Head of Institute, Institute of Aerodynamics and Gas Dynamics, Pfaffenwaldring 21

American Institute of Aeronautics and Astronautics

the model support system and the tunnel walls. Thus, the results require careful application of corrections for these factors to ensure comparability.

The wind tunnel support system's size is determined by the fact that substantial structures are needed in order to precisely orient the model under the influence of possibly significant aerodynamic loads. The system is usually also tasked with traversing the model, for instance to vary the angle of attack. The resulting support system may be large and introduce non-negligible blockage. The model support employed in the present case is shown in Fig. 1, with the sting and the arc sector visible downstream of the model.

Various authors have contributed to the topic of support interference in wind tunnels, including but not limited to Cartieri et al.,[1] Schimanski et al.[2] and Heidebrecht.[3] Additionally, projects such as FLIRET[4] were conducted in order to acquire an understanding of the effects and to develop optimized support systems. Specifically, Stojanowski et al.[5] and Mouton[6] focused on support interference at transonic conditions. More recently, Kohzai et al.,[7] Rivers et al.[8] and König et al.[9] studied the impact of the support system on the Common Research Model at transonic conditions in different transonic wind tunnels.

The near-field effects of a support system can be assessed by performing multiple test runs using different stings in order to fully isolate the influence. Without such runs, separating the support system effects from the model aerodynamics becomes challenging. Such a situation occurred during the European Strategic Wind Tunnel Improved Research Potential (ESWI$^{\text{RP}}$) measurement campaign, a research activity funded by the European Commission's 7th framework program. The authors of this work encountered the issue during the preparation for unsteady computations at high angles of attack,[10–12] revealing differences in force and pitching moment coefficients between experiments and CFD. This motivated the present study, with the goal being the understanding and quantification of the differences between simulation and measurement results.

Rivers et al.[8] studied such phenomena at transonic speeds, using the same aircraft model with a different support sting and a different wind tunnel. A systematic comparison of CFD data and measurements performed in the National Transonic Facility (NTF) revealed significant contributions of the model deformation and the support system to the deviation between experimental and computational results at $M_\infty = 0.85$. To the authors' knowledge, there has been no similar investigation of such effects on the CRM at subsonic Mach numbers and the comparatively high Reynolds number encountered in the ETW campaign. The present study aims to rectify this.
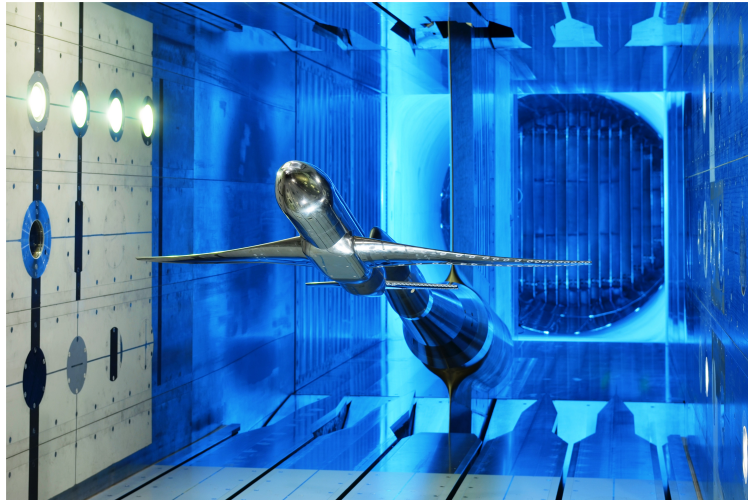

Figure 1. CRM mounted in the ETW,[10] support structure visible in the background

Section II of this work contains an overview over the wind tunnel campaign and gives an introduction into the nature of the support system's influence. The wind tunnel model is described therein as well. The following section describes the computational setup including the grid and solver. Section IV describes the various influencing factors that are expected to impact the results. The computational data is presented in Section V.

American Institute of Aeronautics and Astronautics

II. Background

II.A. Wind Tunnel and Support System

The wind tunnel campaign mentioned above took place in February 2014 at the European Transonic Wind-tunnel (ETW) in Cologne. Among the goals was the study of a modern transport aircraft configuration at flight-like Reynolds and Mach numbers. This necessitated a transonic facility such as the ETW. This is a pressurised, cryogenic closed-circuit wind tunnel capable of testing models at Mach numbers ranging from 0.15 to 1.35. The model for the campaign was provided by the National Aeronautics and Space Agency (NASA). The campaign encompassed a range of Reynolds and Mach numbers, both in the transonic and subsonic regions. An overview of the measurement campaign and related computational studies is given by Lutz et al.[10]

Wind tunnel measurements and CFD simulations typically do not replicate identical inflow conditions. In most cases CFD users seek to obtain data at free-flight conditions without the additional complication and expense of simulating the surrounding wind tunnel infrastructure. Wind tunnel walls and the support system impact the results however, which gives rise to various correction methods in order to achieve comparability of data. A large body of literature addressing the various error sources and corrections has emerged over the past decades, such as the AGARDograph 109[13] or AGARDograph 336.[14]

The wind tunnel walls and their developing boundary layers introduce blockage effects, affecting Mach numbers in the test section and introducing deviations with respect to free flight conditions. Porous walls or slotted walls such as in the ETW serve to mitigate the wall effects, and the corresponding correction methods are well proven. Mokry[15] summarized the wall influence as "low perturbation effects", accessible via linearized potential methods. The wall effects will not be considered separately in this work, as the measurement data includes the corresponding corrections. Gorbushin et al.[16] investigated the wall effects in the context of the ESWI^{RP} campaign in more detail.

According to Stojanowski et al.,[5] the support system's effect may be broken down into a near-field and a far-field contribution. Britcher et al.[17] described a similar classification, recognizing three contributing components: an overall effect, a local flow disturbance and a geometrical distortion of the model. The overall, or far field effect largely stems from the pressure gradient that is introduced by the presence of the support in the test chamber, altering the pressure distribution around the model as well as the resulting forces. It alters the Mach number by slowing down the flow upstream of the support system, necessitating the Mach number correction mentioned above. The local, or near field effect is caused by the interference of the support system with the flow near the model, e.g. by protruding into boundary layers around the model body. This also alters the pressure distribution, but may additionally cause effects such as flow separation. The effect arising from the model modification is due to e.g. missing surfaces at the location of the interface between model and support system. The latter effect is difficult to decouple from the local effect described above and is rarely explicitly determined.[18]

ESWI^{RP}'s outcome consists of several datasets with various levels of corrections applied. The present investigation employs data that was corrected for wall interference, flow curvature and Mach number effects, i.e. a correction that adjusts the Mach number at the model reference point. A sting buoyancy correction is also available to partly account for the support system for comparisons with computations not including the support system, as used in the DPWs. This latter correction mainly alters the drag coefficient and was not considered in the present work, as a more general understanding of the support system's effects was desired.

The support system employed in the ETW campaign can be seen behind the CRM in Fig. 1. A fin sting was used that enters the model fuselage in place of a vertical tail. As shown in Fig. 2, the support diameter increases downstream until it reaches its maximum diameter. Fig. 2(b) gives an impression of the relative diameters of the CRM and the sting as represented in CFD.

II.B. Wind Tunnel Model

The Common Research Model (CRM) had been selected for the ESWI^{RP} measurements in the ETW to represent a contemporary transonic commercial transport. It has been widely used in this capacity for various studies in different fields of aerodynamics research. The 4th[19] and 5th AIAA Drag Prediction Workshops[20] employed it. Various other publications using the CRM have appeared in the past several years, including fluid-structure simulation (Keye et al.[21]), combined wind tunnel and CFD studies (Rivers et al.,[8] Lutz et al.,[10] Waldmann et al.[11]) and many more.

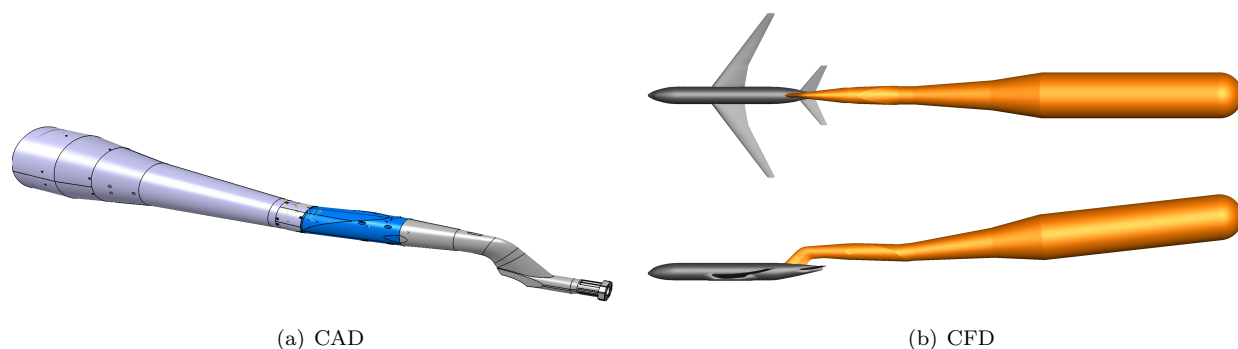American Institute of Aeronautics and Astronautics

(b) CFD

Figure 2. Support system

The wind tunnel model used in the ETW is a 2.7% scale model of the CRM with a wingspan of 1.586 m. The model's horizontal tailplane was set to the neutral position (0°) and no nacelles were mounted on the wings. The model does not have an actual vertical tail plane, its space being occupied by the connection to the support system (cf. Fig. 2(b) showing a representation of the support structure). No transition fixing was employed in the experiment, since fully turbulent flow was assumed due to the large Reynolds number.

The present investigation focuses on results obtained in the subsonic regime at $M_\infty = 0.25$. The relevant runs at that Mach number were carried out at two different wind tunnel operating points: $Re_\infty = 11.6 \cdot 10^6$ (Run 316) and $Re_\infty = 16.85 \cdot 10^6$ (Run 251). This required a temperature of 115 K and a total pressure of 303 kPa and 445 kPa in the wind tunnel, respectively. This lead to normalized dynamic pressure values of $q/E = 0.0674$ resp. $q/E = 0.0987$. Global forces and moments, static wing pressure and deformation were all recorded during the measurement runs. Wind tunnel wall pressure was also recorded for the purpose of wall interference correction.

III.   CFD setup

III.A.   Grid

The baseline geometry is the WBT0 configuration of the CRM including the horizontal tail plane, as used during DPW-4. A semi-span grid created in Pointwise V17.3 was used, as no slip angle variation was considered in the present work. The grid is part of a grid family thas has been extensively used in various works at IAG.[11,12] Its baseline version has been described by Gansel et al.[22] It is a hybrid grid consisting of tetrahedra, with boundary layers resolved by prism and hexahedron layers. The boundary layer grids are adapted to the local flow conditions, so as to achieve a smooth distribution of y^+ over the surface in the presence of a boundary layer that grows with downstream distance. The growing layer height is shown in Fig. 3. The present grid is built with a first cell height of around $y^+ = 0.4$, making it suitable for both linear eddy viscosity models as well as Reynolds stress models. Between 55 and 70 layers were used for boundary layer resolution, with a typical growth rate of about 1.19.
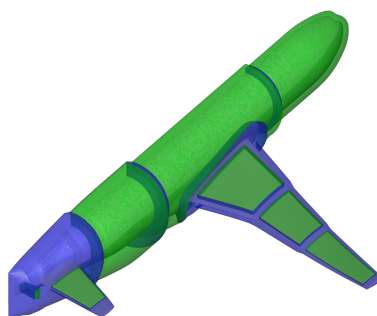

Figure 3. Baseline CRM surface grid topology: hexahedra shown in blue and prisms in green

American Institute of Aeronautics and Astronautics

The geometry contains several junctions forming concave corners, which are typically difficult to resolve properly. One example is the grid in the wing-body intersection, which is known to impact the prediction of the corner flow as highlighted by Sclafani et al.[23] or Brodersen et al.[24] Proper resolution of such areas is therefore crucial. Highly resolved collar-type hexahedral blocks are employed to resolve such regions in the present CRM grid, which avoids chopped cells and acute angles. This approach is also used at the intersection between the tailplane and fuselage as well as the intersection between the support system fin and the rear fuselage of the CRM.

Apart from the baseline WBT0 configuration the study required grids of the CRM with the support system. This configuration is termed WBT0ss. The grid sizes range from 13.7 million nodes for the WBT0 half-model to 17.6 million nodes for WBT0ss. This node count roughly corresponds to the medium resolution range from DPW-4. The grid does not include the model interior or any gap between the model and the fin, with the impact of the model internal flow assumed to be negligible.

III.B.   TAU solver

The computational results presented in this work have been obtained using the Reynolds-averaged Navier Stokes solver TAU, which is an edge-based unstructured solver developed by the German Aerospace Center (DLR).[25] Version 2014.1 of the solver was employed. A second-order central differencing scheme was used for spatial discretization, with a Jameson-type model for artificial dissipation.[26] Most computations cases were started using a first order upwind scheme, successively switching towards higher accuracy methods. The matrix version of TAU's artificial dissipation was included in order to attain the desired accuracy. However, slightly higher dissipation settings than usual were selected in order to be able to use the same settings across the different turbulence models while ensuring computational stability. A lower-upper symmetric Gauss-Seidel scheme was employed for the linear solver. Computations using the Spalart-Allmaras (SA) model were conducted using a CFL number of 5, while the Reynolds stress model (RSM) runs required a value of 2. A multigrid approach with a 5w cycle was applied in all cases.

The one-equation SA model was used for most computations, including all polars. This model remains the mainstay for this type of computations and allows relatively quick simulation times due to requiring the solution of only one additional transport equation. In addition, results using a Reynolds stress model were obtained for the flow condition at $\alpha = 5°$. Only one angle of attack was investigated due to the significantly increased computational effort associated with the application of RSM. The chosen model was SSG/LRR-g, which is a combination of the Speziale-Sarkar-Gatski and the Launder-Reece-Rodi models implemented in TAU.[27] The flow was assumed to be fully turbulent.

A typical feature of eddy viscosity models such as SA is their difficulty to properly resolve corner flows, due to the underlying Boussinesq's assumption and the inability to model anisotropy that arises from it. Specifically, the size of the predicted side of body separation at the rear end of the wing-body junction was highlighted in the 5th Drag Prediction Workshop.[20] Higher-fidelity models such as variants of SA that employ quadratic constitutive relation (Sclafani et al.[23]) and Reynolds stress models (Togiti et al.[27]) can be expected to yield better results. The locally highly resolved grid used in this work enabled the resolution of anisotropic structures in such regions.

IV.   Computational investigation approach

The grids described above formed the basis of the following investigation. With regard to the methodology and setup of the computational cases, several aspects have been identified that may contribute to the deviation between wind tunnel results and CFD data. These are presented in this chapter. For the sake of clarity during the discussion, the difference between the experimental data and the computational results shall be referred to as error. This work does not attempt to appraise the accuracy of the experimental results, the wording is chosen purely for convenience.

IV.A.   Baseline and force integration

The geometry modification aspect as described by Britcher et al.[17] is quantified in this section. The CRM in its baseline configuration (WBT0 in this study) does not include a vertical tailplane, the fuselage is watertight. This is the configuration used in the DPWs and most other computational studies. On the other hand, the wind tunnel model has an opening with the shape highlighted in Fig. 4, which allows the support

American Institute of Aeronautics and Astronautics

sting to enter the fuselage. Hence, even when not taking into account the pressure field modification caused by the fin sting entering the aft fuselage, the typical CFD approach introduces a geometrical deviation in the form of the fin footprint on the fuselage. In the wind tunnel this surface does not exist and does not contribute to the aerodynamic forces acting on the model, a fact which is typically not separately considered in most studies. There is some justification to this, as the area of this part constitutes only about 0.33% of the total model surface.
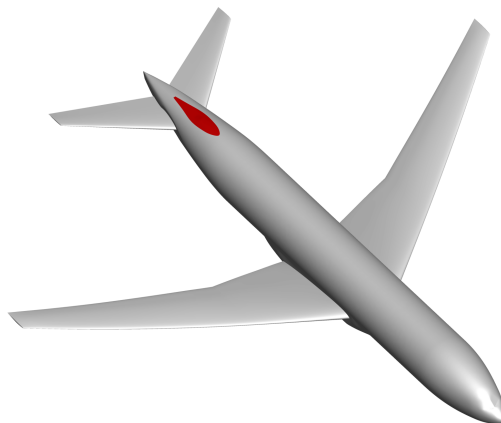

Figure 4. Cover surface on CRM fuselage (highlighted)

Still, there is some benefit to be gained in estimating an order of magnitude for the error introduced by this simplification. To this end, forces and moments were calculated by integrating the surface pressure over the entire baseline surface (both red and green surfaces in Fig. 4). These values, and the same values after subtraction of the cover surface, are presented in Tab. 1. The differences in the last row indicate that the contribution of this surface to the overall lift is very small. However, this surface has a disproportional impact on the pitching moment. This is caused by its far aft position and horizontal orientation, which generates a non-negligible moment around the pitch axis and leads to the deviation in pitching moment of almost 1.8% between the two configurations. The absolute difference remains relatively stable over the angle of attack range, causing a larger relative error at lower α values where the absolute forces and moments are small. While this is clearly not the decisive contributing factor to the overall deviation between CFD and experiment, it should be kept in mind for future studies. For the sake of comparability to previous works, the results for the baseline shown hereafter include the cover surface in their force calculations, i.e. the fully closed geometry is used.

Table 1. Force and moment coefficients obtained by surface pressure integration with and without the cover surface at $\alpha = 1°$, $\alpha = 5°$ and $\alpha = 9°$

	$\alpha = 1°$		$\alpha = 5°$		$\alpha = 9°$	
	C_L	C_{M_y}	C_L	C_{M_y}	C_L	C_{M_y}
baseline	0.2453	0.0239	0.6284	-0.1113	0.9937	-0.2338
without cover	0.2447	0.0256	0.6277	-0.1094	0.9930	-0.2315
delta	0.256%	6.708%	0.111%	1.769%	0.080%	1.006%

IV.B.   Support system size

As described in Section II.A, the support system extends far downstream from the model. A preliminary study was conducted with the goal to establish how much of its actual extent needs to be modeled in CFD. The comparisons in this section were conducted using the baseline wing, i.e. without aeroelastic deformation.

American Institute of Aeronautics and Astronautics

In the wind tunnel, the support sting shown in Fig. 2(a) is mounted to a large arc sector, which is seen far behind the model in Fig. 1. This arc sector was included in simulations by Rivers et al.[8] at transonic conditions, who showed that it has very little influence on the results considering the additional expense necessary to represent it in CFD. Therefore the authors of the present study decided to omit this part, instead focusing on the support sting itself. Three different configurations were modeled, as shown in Fig. 5.
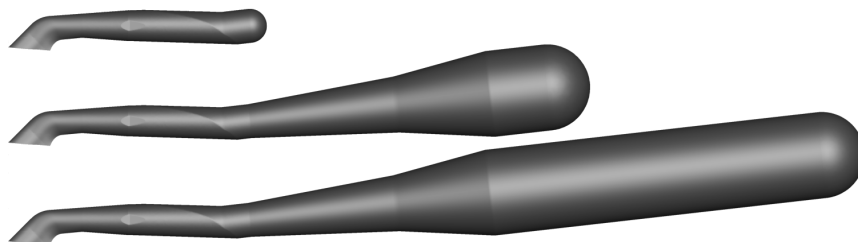

Figure 5. Support system sizes

The small support represents the part immediately behind the fuselage, comprising the fin and the upper swept strut. It can be reasonably expected that this version captures most of the near-field impact on the rear fuselage flow. The medium version additionally models the conical structure (stub sting) downstream of the upper swept strut, which is angled by 6.43° with respect to the horizontal. The length of this medium version roughly corresponds to the actual support up to the sting boss and the arc sector, as seen in Figs. 1 and 2(a). In other words, this version most closely represents the actual wind tunnel structure. At its widest point, the cylindrical part at the end reaches the maximum diameter of $445mm$. The interface between the cylindrical sting and the arc sector was not modeled, instead the cylinder is terminated by a simple hemispherical cap at the downstream end. This was done for the sake of simplicity.

Such a shape can be expected to generate a significant flow separation at its base. A third, even larger, support structure was modeled for comparison in order to minimize the impact of such separation on the pressure field upstream. It was created by extending the medium configuration further downstream at a constant diameter. This type of configuration was used by König et al.[9] The resulting force and moment coefficients at $\alpha = 5°$ listed in Table 2 show a significant difference in all coefficients between the small and medium configuration, whereas the larger one does not lead to significantly different results than the medium one. This leads to the conclusion that the displacement caused by the increasing cross-section of the structure behind the model is a significant influencing factor for the overall pressure field around the model. The large version does further improve the results to a certain extent, however it apprears not to be worth the grid size increase and additional computational effort. For this reason the present work focuses on the medium configuration.

Table 2. Force and moment coefficients using different support system sizes at $\alpha = 5°$, no aeroelastic deformation

	C_L	C_D	C_{M_y}
small	0.6098	0.0290	-0.0713
medium	0.6074	0.0284	-0.07000
large	0.6065	0.0283	-0.0690

IV.C.   Wing deformation

The flow in a pressurised cryogenic wind tunnel imposes significant aerodynamic loads on the model, which lead to non-negligible deformation. This mainly affects the wing and the tailplane. A swept wing bends upwards and twists when generating lift, with the twist increment increasing the washout and thereby unloading the outboard part. As established by Rivers et al.,[8] the shape of the CRM wind tunnel model as manufactured corresponds to an aeroelastic deformation at 1g load condition. This shape further deforms

American Institute of Aeronautics and Astronautics

when subjected to loads in the wind tunnel. These bend and twist increments were measured by an optical stereo pattern tracking system in the ETW, providing deformation data at discrete spanwise stations. The scaled distributions are shown in Fig. 6.

While the present CFD investigation focuses on Run 316, the deformation measurement system was not active during that particular test run. Deformation data obtained during Run 256 (at $Re_\infty = 16.85 \cdot 10^6$) is used instead. The difference in dynamic pressure q/E between these operating points affects the loads and deformations. This effect is taken into account by proportionally scaling the bend and twist distributions using q/E, as shown by Illi.[28] The HTP deforms under load as well, the magnitude is however very small. This deformation was neglected in the present investigation.
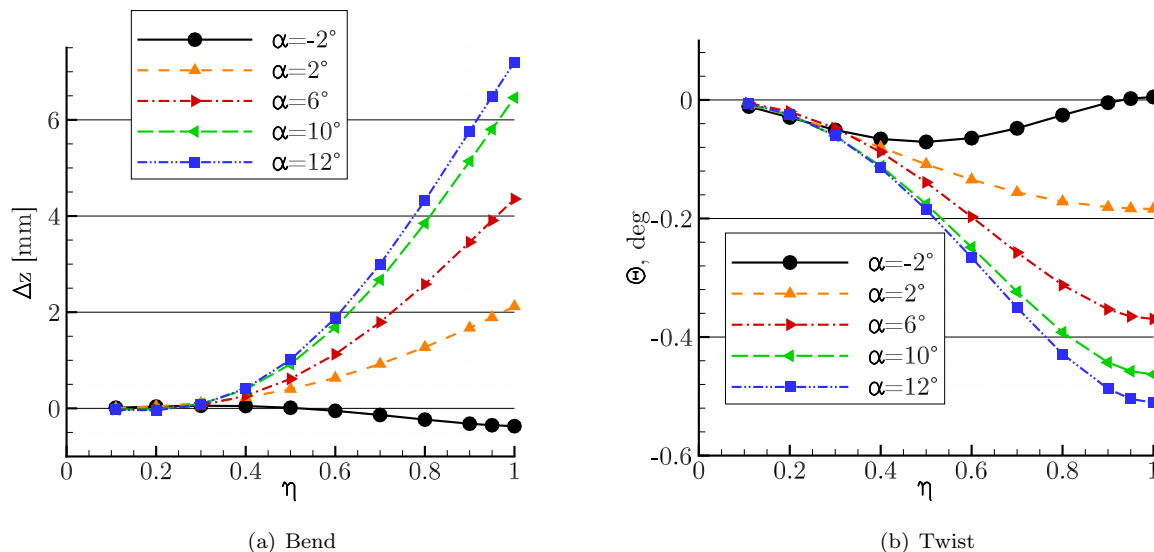

(a) Bend   (b) Twist

Figure 6. **Bend and twist increments relative to model shape, scaled to** $Re = 11.6 \cdot 10^6$

Previous studies focusing on transonic operating points indicated that the impact of wing deformation is rather large. This can be attributed to the sensitivity of the shock position to the local angle of attack, with the latter being modified by local wing section twist. A shifted shock significantly alters the pressure distribution and thereby the lift and drag. This effect is absent at the present subsonic conditions. It can be reasonably expected that the deformation will have a much more gradual effect which will be modest in its magnitude, in comparison to transonic cases. The highest observed twist at the tip is on the order of 0.5° in this case. The wing also deflects upwards by up to $7mm$ at the tip, which corresponds to just 3.7 % of the mean aerodynamic chord.

The computational grid was built for the undeformed shape of the wind tunnel model described above. The bend and twist increments were applied to the grid by shifting the grid nodes, without affecting wall spacings and growth rates. The process has been described by Illi.[28] This minimizes grid effects between angles of attack, ensuring that the same grid layout and topology is used at every point in the polars. Deformation was only applied to the grid including the support system (WBT0ss). The deformed data sets shall be termed WBT0ssd.

V.   Computational Results

In the following, computational results of the three configurations will be presented, including experimental data where appropriate. The undeformed baseline case (WBT0), the undeformed case including the medium support system from Section IV.B (WBT0ss) and the same configuration including aeroelastic wing deformation (WBT0ssd) form the dataset for the investigation. First an overview of the observed differences in the global force and moment values between the various configurations will be given. Wing pressure distributions will be evaluated to understand the differences in lift prediction in more detail. At the end, the effect of the support system on the flow in the vicinity of the tail will be evaluated and the effects of the Reynolds stress model will be described.

American Institute of Aeronautics and Astronautics

V.A.   Forces and Moments

A comparison of the force and moment coefficients between the three configurations is shown in Fig. 7. The baseline values match the slope of the lift curve and the overall shape, albeit with a consistent offset towards higher lift values. Similar behavior can be observed in the drag and pitching moment polars. These are similar to what was observed in the DPW summaries[19] as well as reported by other authors,[89] for transonic conditions. There is no known published computational data at $M_\infty = 0.25$ for comparison at the time of writing, thus only the ETW results serve for comparison. The simulation results shall be evaluated in terms of error with respect to the experimental data. All computational results overpredict both lift and drag, while the computed pitching moment tends to more negative values than the experimental data. The results obtained with the medium support system improve the predictions of all coefficients, as had been expected. For instance, the error in C_L at $\alpha = 5°$ is reduced from 0.042 to 0.018. Adding the wing deformation further improves the CFD prediction by lowering the lift. Using the Reynolds stress model is also beneficial for lift prediction, as shown in the inset of Fig. 7(a). The RSM effects will be addressed at the end of this chapter.
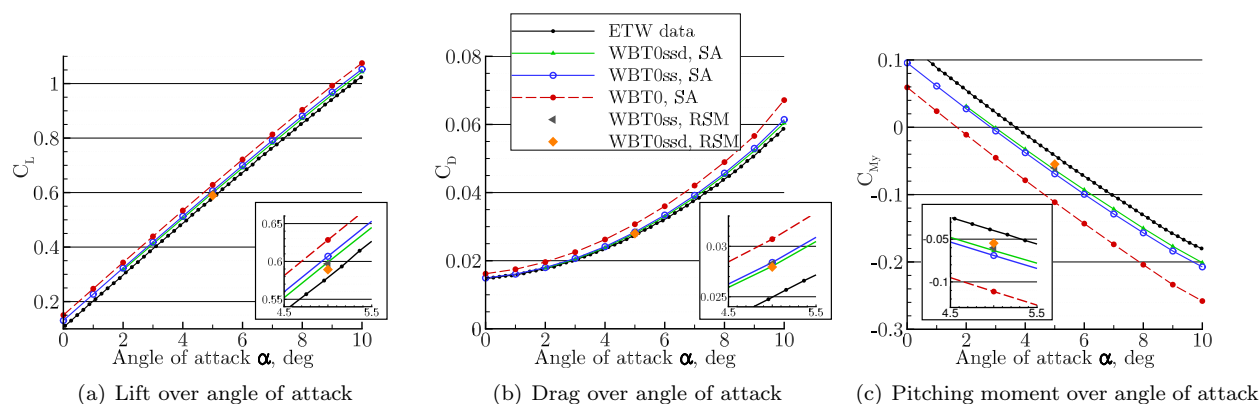

(a) Lift over angle of attack   (b) Drag over angle of attack   (c) Pitching moment over angle of attack

Figure 7. Force and moment polars with and without support system at $\mathbf{M_\infty = 0.25}$, $\mathbf{Re = 11.6 \cdot 10^6}$

The baseline drag prediction diverges from the experimental value with increasing angle of attack, ΔC_D increasing from 52 drag counts at $\alpha = 5°$ to 110 drag counts at $\alpha = 10°$. The inclusion of support system and wing deformation shows a strong effect, reducing the error over the entire angle of attack range. The error in C_D at $\alpha = 5°$ is reduced by 27 drag counts (to 25), with the reduction increasing to 67 drag counts at $\alpha = 10°$ (to 43). Wing deformation has very little impact on C_D, improving the result only slightly. The Reynolds stress model further improves the results somewhat, however the support system effect is clearly the main driver behind the error reduction.

The pitching moment coefficient in Fig. 7(c) shows again an offset from the experimental values which increases slightly with angle of attack. A significant reduction of the deviation is achieved by including the support system in the calculation. Wing deformation also improves the result, especially at higher angles of attack. This is caused by the the lower lift on the outboard wing, which decreases the nose-down moment generated by these regions. This effect will be described in more detail below. Similarly, the SSG/LRR-g model's predictions are closer to the measured values. Overall, ΔC_M is reduced from 0.069 at baseline to 0.021 for WBT0ssd at $\alpha = 5°$.

In effect, the inclusion of the support system, wing deformation and the application of an anisotropy-resolving turbulence model all contribute to reductions of the errors in the force and moment coefficients to varying degrees. The best solution is attained by the WBT0ssd configuration with the SSG/LRR-g model. At $\alpha = 5°$ this best case achieves an error reduction of 76%, 55% and 78% for C_L, C_D and C_M, respectively, from the baseline. The influencing factors making up this reduction can be broken down into their relative contributions to the total error reduction at that angle of attack, as listed in Table 3. The support system is responsible for the largest difference with respect to the baseline, contributing over half of the total error reduction in all cases, reaching 82% in the drag coefficient. The turbulence model mainly impacts the lift and pitching moment. The wing deformation is similar in that regard, with an additional contribution to drag reduction.

Table 3. Relative weights of support system, wing deformation and Reynolds stress model with respect to overall error reduction at $\alpha = 5°$. Values are percentages.

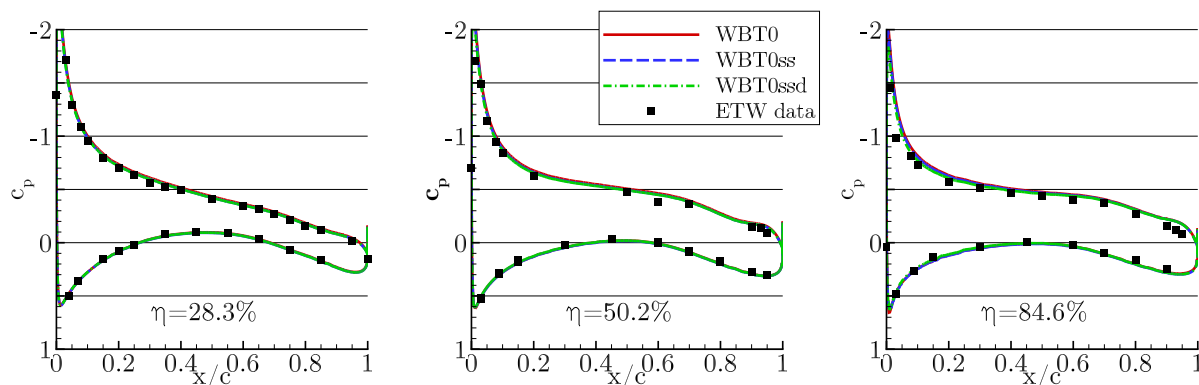|	C_L	C_D	C_M
support system	53	82	73
wing deformation	22	14	12
RSM	25	4	15

Figure 8. Wing pressure distributions with and without support system $\alpha = 5°$, $M = 0.25$, $Re = 11.6 \times 10^6$

V.B.   Wing Pressure Distribution

The wing pressure distributions in Figs. 8 and 9 show the comparison between the various CFD runs and the measurements. The agreement between experiment and CFD is very good at the inboard stations, with the pressure levels and suction peak shape well reproduced by the simulations. Also, these inboard stations show the least spread between the different CFD configurations. The difference increases further outboard, especially the twisted wing (WBT0ssd) exhibiting the largest deviation from the other simulation results and moving closer to the experimental data. Still, all simulations overpredict the lift at the outboard stations, which is likely responsible for the difference in overall C_L. The observations do not change with angle of attack.

Generally, the findings with respect to pressure distribution and forces are in line with the results obtained by other authors such as König et al.[9] and Yasue et al.[29] In all cases significant improvement of the simulation results can be achieved by including the support system and the wing deformation in the calculation, however there is still some residual error. This may be attributed to insufficient grid refinement, turbulence model inadequacies, or possibly the fact that the fully turbulent computation may not reflect the wind tunnel situation. Since the present work does not include a grid refinement study, a quantitative analysis of the exact error sources shall not be attempted.

The difference in spanwise C_L distributions between the simulated configurations is visualised in Fig. 10. The comparison neatly summarizes the effects of the sting and the wing deformation. The curves for WBT0 and WBT0ss are shifted by some amount over the entire wing, with slightly higher lift seen in WBT0. The difference diminishes towards the wing tip. The wing deformation is small at the root and increases further outboard, which leads to an increasing drop in local lift towards the tip.

Compared to the studies at transonic conditions cited above, the effect of the support system and the aeroelastic deformation on the wing pressure distribution appears comparatively small. This may be explained by the absence of a shock on the suction side, whose position would be highly sensitive to the local flow angle and inflow Mach number, both of which would be altered by the support system and wing twist. The subsonic pressure distributions encountered here vary smoothly with the pressure field changes induced by these factors. The wing deformation effect is also less pronounced, simply due to the fact that the wing is less deformed by the lower dynamic pressure than in the transonic case.
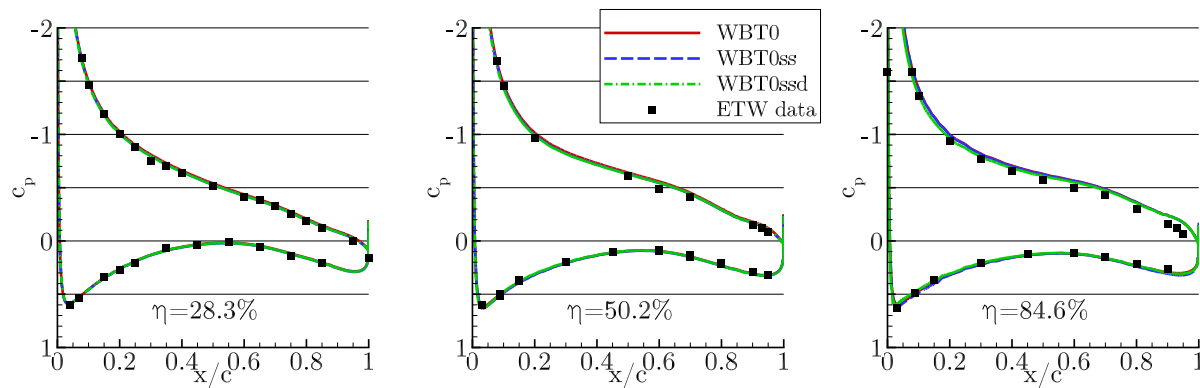
American Institute of Aeronautics and Astronautics

Figure 9. Wing pressure distributions with and without support system $\alpha = 9°$, $M_\infty = 0.25$, $Re = 11.6 \times 10^6$
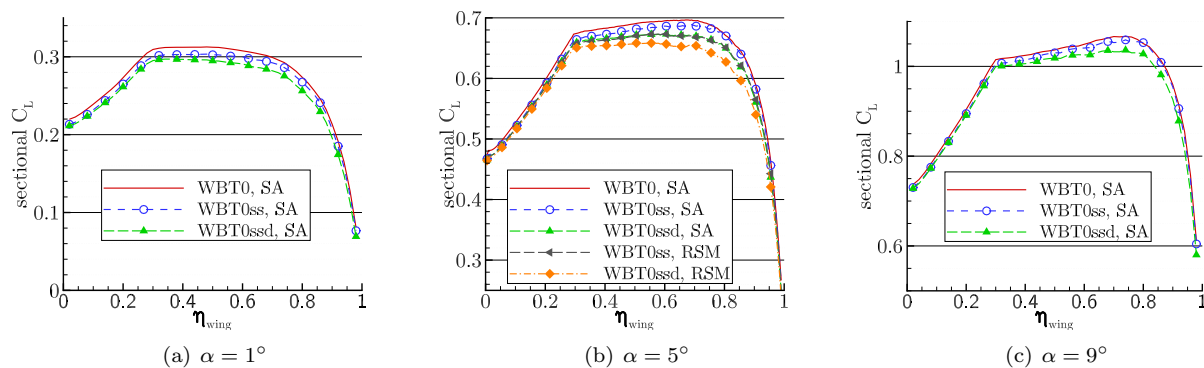

Figure 10. Sectional wing lift distributions with and without support system

Nonetheless the results clearly indicate a decrease in overall lift when taking into account the support system. The lift decrease on the inboard wing due to the support system is likely a manifestation of its far field effect, influencing the pressure field around the model. This effect is strongest at the centerline and diminishes outward, which is reflected in Fig. 10.
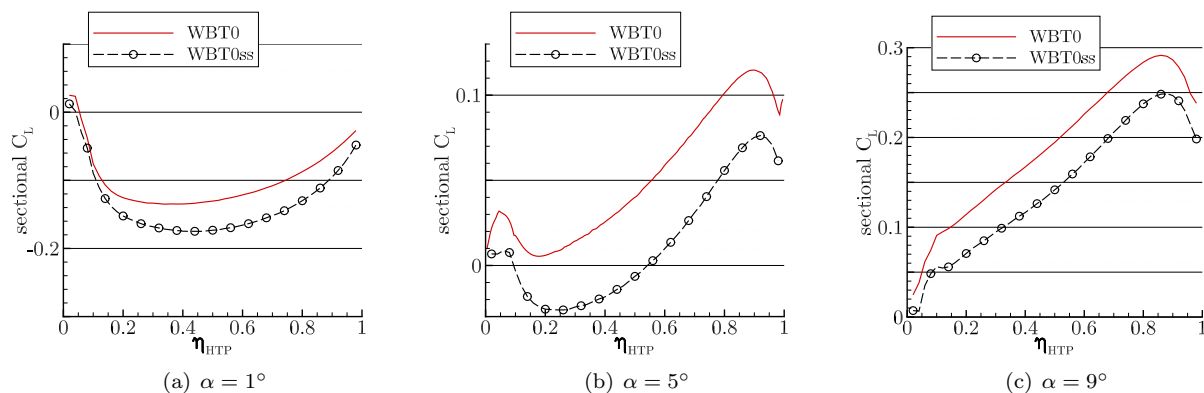
V.C.   Tail Flow and Sting Near Field Effect

The differences in wing pressure distribution alone do not fully explain the entire deviation between the baseline and WBT0ss/WBT0ssd. Table 4 shows a breakdown of the model parts' contributions to the overall C_L for the baseline and WBT0ss at $\alpha = 5°$, indicating decreases everywhere. The values are lift coefficients calculated using the wing reference area. The wing is strongly affected, however the fuselage and horizontail tailplane also show drops in the lift force. These are likely due to near field effects of the support system.

The HTP pressure distribution shown in Fig. 11 is an indication of this. The plots show the sectional load on the HTP using the wing mean aerodynamic chord as reference. The lift generated by the tailplane decreases markedly in the presence of the support system. The cause of this is a high pressure region over the upper side of the HTP generated by the mounting system. The lower HTP lift is consistent with the reduced nose-down pitching moment - a stronger downward force in the tail region lowers the overall lift while causing the aircraft to pitch up.

The pressure difference between WBT0 and WBT0ss at the rear of the CRM is shown in Fig. 12(a) for $\alpha = 5°$, with $\Delta c_p = c_{p,WBT0ss} - c_{p,WBT0}$. There is some pressure rise due to deceleration in front of the support, as well as the opposite effect due to the acceleration along the fin base on its sides. There is a second high pressure region behind the fin sting, which contributes to C_D reduction by decreasing the base

American Institute of Aeronautics and Astronautics

Table 4. Breakdown of C_L contribution at $\alpha = 5°$, no wing deformation

	WBT0	WBT0ss
fuselage	0.0789	0.0724
wing	0.5407	0.5334
HTP	0.0088	0.0010
total	0.6284	0.6068

(a) $\alpha = 1°$ (b) $\alpha = 5°$ (c) $\alpha = 9°$

Figure 11. Sectional HTP lift distributions with and without support system

drag of the fuselage. Contours of pressure difference in the symmetry plane (Fig. 12(b)) clearly show the high pressure regions at the rear and above the fuselage. In combination with the increased HTP lift, these areas of elevated pressure contribute to a higher nose-up pitching moment due to their large moment arm. This pressure distribution significantly shifts the predicted C_M towards the experimental results, as observed in Fig 7(c).

V.D.   Effect of the Turbulence Model

Forces and moments obtained with the SSG/LRR-g model on the WBT0ss and WBT0ssd configurations at $\alpha = 5°$ shown above in Fig. 7(b) indicated that the Reynolds stress model yields superior results compared to the SA model. The Reynolds stress model predicts slightly lower drag and lift at that flow condition. This is mostly due to lower lift predicted by RSM in the outboard region of the wing, as shown in Fig. 10(b) and in terms of Δc_p in Fig. 13(a). This corroborates the findings of Togiti et al.,[27] who also found that the SSG/LRR-g model predicts lower lift values than the eddy viscosity model. The lower outboard lift also explains the improved C_M prediction, as the outboard region of the swept wing is located behind the moment reference point. Lower lift in that region contributes to a decreased nose-down moment. Fig. 13(b) shows further differences between the two models in the tail region. Both junctions show elevated values of Δc_p, which indicates the presence of horseshoe vortex-like structures in the RSM solution.

Contrary to the computations in the transonic regime mentioned in Section III.B, there is no large scale separation at the wing-body junction. The separation region predicted by the Spalart-Allmaras model is already very small, with little variation over the angle of attack range. The SSG-LRR/g model exhibits a smaller separated region still, as shown in Fig. 14(a). The small but noticeable difference between SA and RSM results is also evident at other locations such as the tailplane-body junction (Fig. 14(b)) and the trailing edge of the fin sting (Fig. 14(c)). In all cases the Reynolds stress model predicts a slightly smaller scale separation, which contributes to the lower drag values obtained with this model.
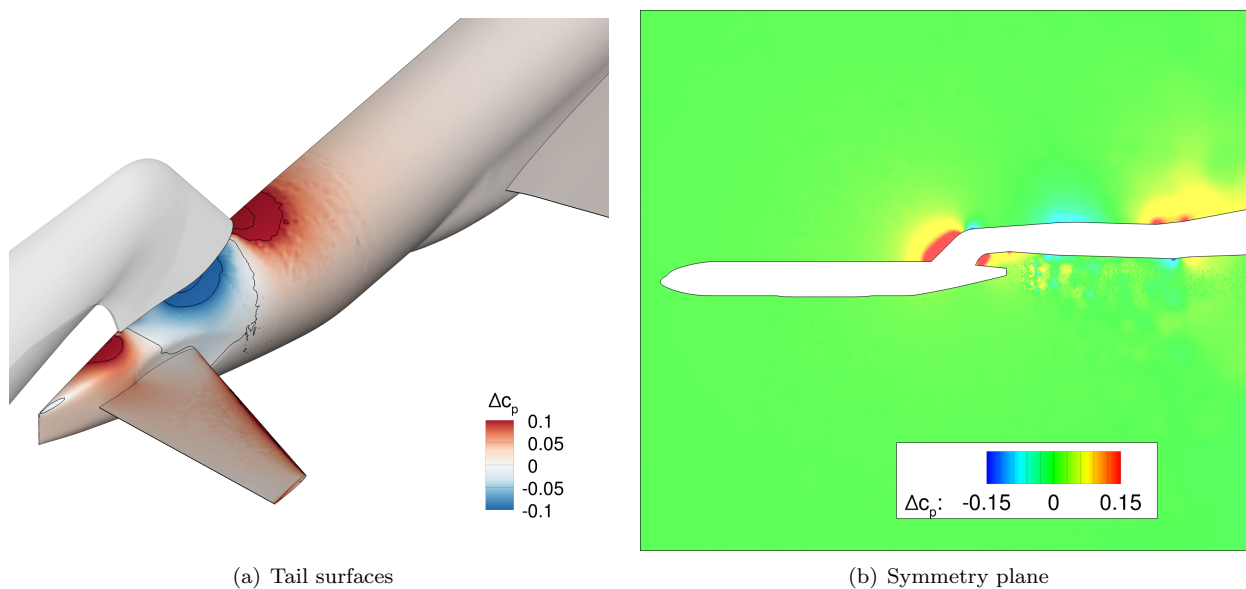
(a) Tail surfaces

(b) Symmetry plane

Figure 12. Pressure difference caused by the support system at $\alpha = 5°$
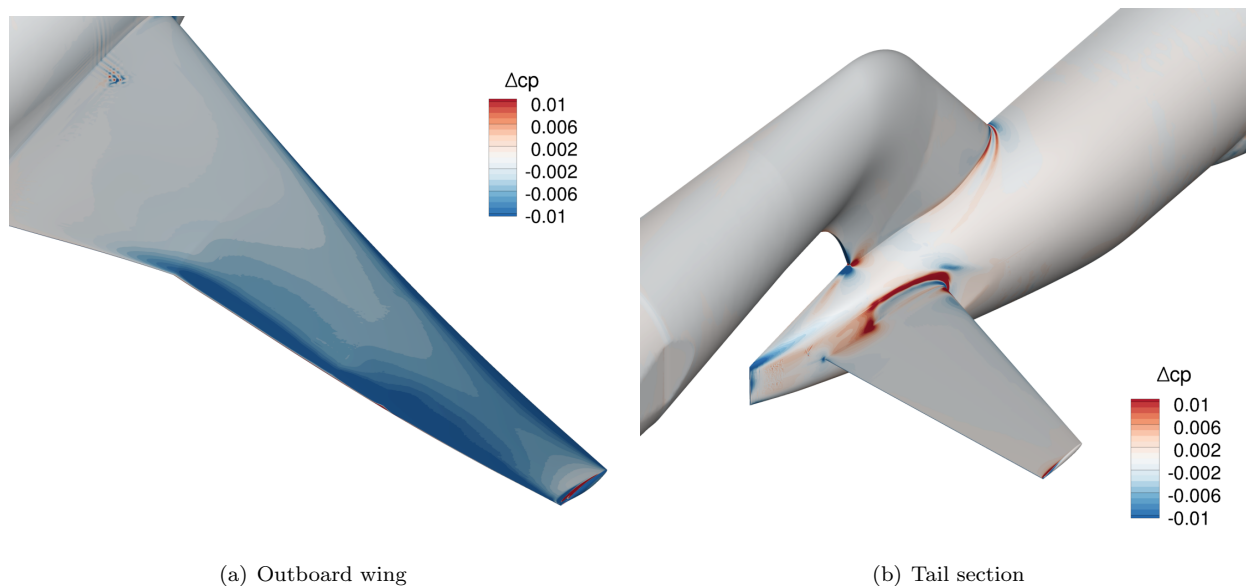

(a) Outboard wing

(b) Tail section

Figure 13. Pressure difference between SA and SSG/LRR-g models (blue: lower c_p in SA), WBT0ss configuration, $\alpha = 5°$
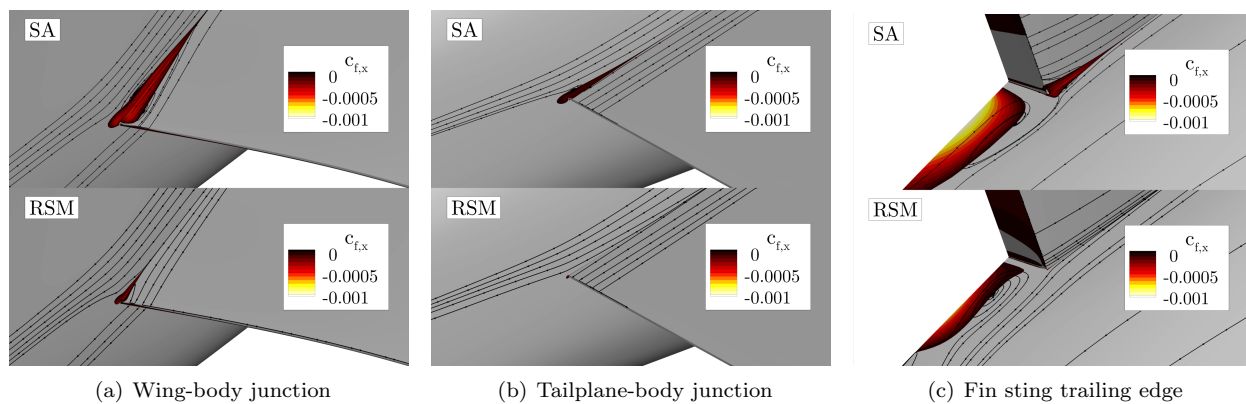

(a) Wing-body junction

(b) Tailplane-body junction

(c) Fin sting trailing edge

Figure 14. Surface streamlines and backflow regions (colored) for SA and RSM at $\alpha = 5°$, WBT0ss configuration

American Institute of Aeronautics and Astronautics

VI.   Conclusion

The present work summarized efforts to quantify the impact of various factors contributing to errors in the simulation results with respect to measurement data of the Common Research Model at subsonic conditions. Computational studies were performed using several geometry variants in order to demonstrate the magnitude of the effect of the support system and other factors on the obtained results. It was shown that the fidelity of the computational results can be improved by taking into account the support system, the aeroelastic wing deformation and by employing a more sophisticated turbulence model than the originally used one equation model.

The extent of the modeled support system that is required in CFD to adequately represent the sting influence on the pressure field surrounding the model were determined. Three different configurations were evaluated at $\alpha = 5°$, concluding that the medium size configuration is sufficient. The contribution of the sting cover surface to the overall force and moment balance was calculated, revealing that omission of the cover contributes to the moment coefficient error.

The support system was shown to have the most significant impact on the results, being especially important for the reduction of the drag coefficient error. Its effect are visible in the near field, where it strongly affects the pressure distribution around the aft fuselage and the tailplane. The local pressure distribution is affected in such a way as to decrease base drag and the tailplane lift. The latter significantly alters the overall pitching moment. The wing deformation primarily affects the outboard lift, which contributes to a lower overall lift. It also descreases the nose-down pitching moment due to the wing sweep. The same effect is observed when the Reynolds stress model is employed, both factors adding up to an improved lift and moment prediction. The RSM also decreases separation in the corners of the model geometry, predicting lower drag overall than the SA model.

Overall, the support system is responsible for over 50% of the achieved error reduction in all three coefficients. The original error between the baseline CFD computations and the experimental results at $\alpha = 5°$ was reduced by 76%, 55% and 78% for C_L, C_D and C_M, respectively by including the support, wing deformation and employing an RSM model. This constitutes an encouraging outcome. However, since no studies on the CRM at the same flow conditions are known, these results need to be seen as a first point of reference. Future studies are needed to determine the causes of the residual errors.

Acknowledgments

References

[1]Cartieri, A., Mouton, S., and Boyet, G., "Study of Support Interference Effects at S1MA Wind Tunnel within the "SAO" Project," *27th Internation Congress of the Aeronautical Sciences*, Sept. 2010.

[2]Schimanski, D. and Quest, J., "Tools and Techniques for High Reynolds Number Testing Status and Improvements at ETW," *AIAA Paper 2003-0755*, Jan. 2003.

[3]Heidebrecht, A., "A numeric far field model for support interference studies in a slotted wall wind tunnel (European Transonic Windtunnel)," *Proceedings of the Institution of Mechanical Engineers, Part G: Journal of Aerospace Engineering*, Vol. 220, No. 6, June 2006, pp. 581–587.

[4]Kuehn, W., "FLIRET Final Publishable Report," Tech. rep., Airbus Deutschland, 2010.

[5]Stojanowski, M. and Germain, E., "The FALCON 7x from ETW to flight," *46th AIAA Aerospace Sciences Meeting and Exhibit, Paper 2008-0835*, Jan. 2008.

[6]Mouton, S., "Numerical Investigations of Model Support Interference in Subsonic and Transonic Wind Tunnels," *8th ONERA-DLR Symposium ODAS2007, Göttingen, October 17-19*, Oct. 2007.

[7]Kohzai, M., Ueno, M., Koga, S., and Sudani, N., "Wall and Support Interference Corrections of NASA Common Research Model Wind Tunnel Tests in JAXA," *AIAA Paper 2013-0963*, Jan. 2013.

[8]Rivers, M. B., Hunter, C. A., and Campbell, R. L., "Further Investigation of the Support System Effects and Wing Twist on the NASA Common Research Model," *30th AIAA Applied Aerodynamics Conference, New Orleans, AIAA 2012-3209*, June 2012.

[9]König, B. and Fares, E., "Validation of a Transonic Lattice-Boltzmann Method on the NASA Common Research Model," *AIAA Paper 2016-2023*, Jan. 2016.

[10]Lutz, T., Gansel, P. P., Waldmann, A., Zimmermann, D.-M., and Schulte, S., "Time-Resolved Prediction and Measurement of the Wake Past the CRM at High Reynolds Number Stall Conditions," *Journal of Aircraft*, Vol. 1, No. 1, 2015.

American Institute of Aeronautics and Astronautics

[11]Waldmann, A., Gansel, P. P., Lutz, T., and Krämer, E., "Unsteady Wake of the NASA Common Research Model in Low-Speed Stall," *Journal of Aircraft accepted for publication*, Vol. 1, No. 1, 2015.

[12]Zimmermann, D.-M., Waldmann, A., Lutz, T., and Krämer, E., "Development of Flow Structures in the Near-Field Wake Region of the Common Research Model," *Challenges in European Aerospace (CEAS 2015), Delft, Netherlands*, Sept. 2015.

[13]"AGARDograph 109, Subsonic Wind Tunnel Wall Corrections," 1966.

[14]"AGARDograph 336, Wind Tunnel Wall Correction," 1998.

[15]Mokry, M., "Evaluation of combined wall- and support-interference on wind tunnel models," *AGARD-CP-535, Paper 28*, Oct. 1993.

[16]Gorbushin, A., Bosnyakov, S., Glazkov, S. A., Llysenkov, A. V., Matyash, S. V., Semenov, A. V., and Quest., J., "Slotted Wall Interference Investigation in ETW using the NASA CRM model," *AIAA Paper 2015-0621*, Jan. 2015.

[17]Britcher, C. P., Alcorn, C. W., and Kilgore, W. A., "Subsonic sting interference on the drag of a family of slanted-base ogive-cylinders," *AIAA Paper 89-2006-CP*, Jan. 1989.

[18]Mackay, M., "A Review of Sting Support Interference and some Related Issues for the Marine Dynamic Test Facility (MDTF)," *Defence Research Establishment Atlantic, DREA Report 93/107*, Oct. 1993.

[19]Vassberg, J. C., Tinoco, E. N., Mani, M., Rider, B., Zickuhr, T., Levy, D. W., Brodersen, O. P., Eisfeld, B., Crippa, S., Wahls, R. A., Morrison, J. H., Mavriplis, D. J., and Murayama, M., "Summary of the Fourth AIAA CFD Drag Prediction Workshop," *AIAA Paper 2010-4547*, June 2010.

[20]Levy, D. W., Laflin, K. R., Tinoco, E. N., Vassberg, J. C., Mani, M., Rider, B., Rumsey, C. L., Wahls, R. A., Morrison, J. H., Brodersen, O. P., Crippa, S., Mavriplis, D. J., and Murayama, M., "Summary of Data from the Fifth Computational Fluid Dynamics Drag Prediction Workshop," *Journal of Aircraft*, Vol. 51, No. 4, 2014, pp. 1194–1213.

[21]Keye, S., Togiti, V., Eisfeld, B., Brodersen, O. P., and Rivers, M. B., "Investigation of Fluid-Structure-Coupling and Turbulence Model Effects on the DLR Results of the Fifth AIAA CFD Drag Prediction Workshop," *49th AIAA Applied Aerodynamics Conference, San Diego, USA*, Jan. 2013.

[22]Gansel, P. P., Illi, S. A., Krimmer, S., Lutz, T., and Krämer, E., "Unsteady CFD Simulation of the NASA Common Re-search Model in Low Speed Stall," *High Performance Computing in Science and Engineering '13*, ISBN 978-3-319-02164-5 2013, pp. 439–453.

[23]Sclafani, A., "Analysis of the Common Research Model Using Structured and Unstructured Meshes," *Journal of Aircraft*, Vol. 51, No. 4, July 2014, pp. 1223–1243.

[24]Brodersen, O., "DLR Results from the Fourth AIAA Computational Fluid Dynamics Drag Prediction Workshop," *Journal of Aircraft*, Vol. 51, No. 4, July 2014, pp. 1135–1148.

[25]Schwamborn, D., Gerhold, T., and Heinrich, R., "The DLR TAU-Code, Recent Applications in Research and Industry," *European Conference on Computational Fluid Dynamics ECCOMAS CFD 2006*, Sept. 2006.

[26]Roe, P., "Approximate Riemann Solvers, Parametric Vectors and Difference Schemes," *Journal of Computational Physics*, Vol. 43, Sept. 1981, pp. 357–372.

[27]Togiti, V., Eisfeld, B., and Brodersen, O., "Turbulence Model Stufy for the Flow Around the NASA Common Research Model," *Journal of Aircraft*, Vol. 51, No. 4, July 2014, pp. 1331–1343.

[28]am Hülse, S. A. S., *Simulation transsonischen Buffets an Transportflugzeugen mittels hybrider RANS-/LES Verfahren*, Ph.D. thesis, Universität Stuttgart, Stuttgart, Aug. 2015.

[29]Yasue, K. and Ueno, M., "Model Deformation Corrections of NASA Common Research Model Using Computational Fluid Dynamics," *Journal of Aircraft*, Jan. 2016.

American Institute of Aeronautics and Astronautics